ISPRS Journal of Photogrammetry and Remote Sensing 80 (2013) 1–9

Contents lists available at SciVerse ScienceDirect

ISPRS Journal of Photogrammetry and Remote Sensing

journal homepage: www.elsevier.com/locate/isprsjprs

On the use of compact polarimetry SAR for ship detection

G.E. Atteia, Michael J. Collins *,[1]

Department of Geomatics Engineering, University of Calgary, Calgary, AB, Canada T2N 1N4

ARTICLE INFO

Article history:
Received 26 March 2012
Received in revised form 20 September 2012
Accepted 8 January 2013
Available online 2 April 2013

Keywords:
Ship detection
Polarimetry
Compact polarimetry
Synthetic aperture radar

ABSTRACT

Quad-pol data are generally acknowledged as providing the highest performance in ship detection applications using SAR data. Yet quad-pol data have half the swath width of single and dual-pol data and are thus less useful for maritime surveillance, where wide area coverage is crucial. Compact polarimetry (CP) has been proposed as a compromise between swath width and polarization information. The circular-transmit-linear-receive (CTLR) CP data have certain engineering advantages over other CP configurations. CP data may be used to reconstruct a reduced quad-pol covariance matrix (termed pseudo-quad, or PQ, data) and the potential of these data in terrestrial applications has recently been demonstrated. We present some of the first results on the use of CTLR data and reconstructed quad-pol data for ship detection. We use Radarsat-2 fine-quad (FQ) data to examine 76 ships over a range of incidence angles and ship orientations at low to moderate wind speeds. We examined the ship detection performance of full quad-pol and full-PQ data; several dual-pol configurations suggested in the literature, *HV* and PQ *HV* and the raw CTLR data. We find that the ship detection performance of the PQ *HV* data is the strongest of all the detectors we examined, with performance that was comparable to quad-pol data. Other strong performers were *HV* and CTLR data.

1. Introduction

The detection of ships in the ocean has a wide range of applications including search and rescue, monitoring illegal activities and routine surveillance of commercial shipping. While shore-based electro-magnetic sensing devices, such as HF radar, may be used to detect ships close to shore, remotely sensed image data offer regular offshore coverage. Synthetic aperture radar, or SAR, with its day-night, all-weather capability, is the preferred data source for monitoring ocean ship traffic.

The history of ship detection with radar goes right back to the very first radar (or telemobiloscope) designed and built by Christian Huelsmeyer (Swords, 1986). In Huelsmeyer's first experiment, on May 18, 1904, he set up his new radar on the Hohenzollern Bridge in Cologne, Germany and was able to detect ships coming down the Rhine. Ship detection was a key application of radar in the military conflicts in the first half of the twentieth century. Although there had been earlier airborne imaging radar systems, it was the launch of Seasat, the first civilian satellite-based SAR, that accelerated the publication of ship detection algorithms in the open literature (Evans, 1979; Gower and Hughes, 1979), an effort which intensified with the launches of ERS-1 and Radarsat-1. These early studies all used single channel SAR imagery (Vachon et al., 1997; Greidanus et al., 2004). With the launch of Envisat ASAR, dual-polarization data became available, and ship detection algorithms using these dual-pol data began to appear (Olsen and Wahl, 2003). These efforts continued with the launch of ALOS-PALSAR, TerraSAR-X and Radarsat-2. Also, two forthcoming polarimetric Earth-observing SARs are scheduled to be lunched in 2012–2013; the Japanese AlOS-2 (Okada et al., 2011), and Argentina's SAOCOM (D'Aria et al., 2008).

The existing polarimetric SAR systems have quad-polarized imaging modes which have proved very effective in ship detection (Touzi et al., 2001; Touzi, 2000). Studies for determining the best polarization combinations composed from the four polarimetric channels (HH, HV, VH and VV) for ship detection were performed by Yeremy et al. (2001), Touzi (1999), Touzi (2000), Liu et al. (2005) and Liu and Meek (2005). These studies showed that quad-pol and dual-pol data often yield higher accuracy than single channel data. While there is little consensus on which single-pol and dual-pol channels offer the best performance, quad-polarimetric systems provide the largest amount of scattering information about targets and lead to the best detection performance over all other SAR systems. However, this performance gain comes at the expense of swath width and system complexity.

In maritime surveillance applications, swath width is of critical importance since one of the objectives of these applications is to

* Corresponding author.
E-mail address: mjcollin@ucalgary.ca (M.J. Collins).
[1] This work was completed while M.J.C. was a visiting research engineer at the Jet Propulsion Laboratory in Pasadena, CA, USA.

0924-2716/$ - see front matter © 2013 International Society for Photogrammetry and Remote Sensing, Inc. (ISPRS) Published by Elsevier B.V. All rights reserved.
http://dx.doi.org/10.1016/j.isprsjprs.2013.01.009

cover as much area as possible to achieve both reliability and economic efficiency. Dual-polarization data offers a balance between swath width and the added accuracy that can often be realized with multiple polarizations. Many studies have reported the performance gain offered by dual-polarization data over single channel data in maritime surveillance (Liu et al., 2005; Liu and Meek, 2005; Howell et al., 2008). However, quad-pol data consistently outperform both single and dual-pol data.

The operational advantages of dual-polarization data have prompted interest in compact polarimetry, or CP, data (Souyris et al., 2005; Raney, 2006). Compact polarimetry is a dual-polarized SAR imaging system that has several important advantages over other multi-polarization SAR systems. As with other dual-polarized SAR systems, CP transmits one polarization and receives two other polarizations. There are currently three CP polarization configurations that have been reported in the earth observation literature. The $\pi/4$ mode transmits a linear polarization that is oriented at 45° to the conventional horizontal and vertical polarizations, and it receives H and V. Dual circular polarization transmits right or left circular polarization and receives both right and left. Finally, circular transmit, linear receive (CTLR), transmits right or left circular polarization and receives H and V. These three CP modes share the advantages of having a greater amount of polarization information than the standard dual-pol linear systems (transmit H or V and receive H and V), while covering twice the swath width of quad polarized SAR systems. However, the CTLR systems have certain engineering advantages that lead to higher quality data (Raney, 2007b; Raney, 2007a).

CP SAR systems have been used in planetary imaging for some time. Most recently, the miniSAR on board Chandrayaan-1 (Raney et al., 2010) collected CP SAR images of our moon (Carter et al., 2011).

Although there are currently one spaceborne CP SAR system available for earth observation (Risat-1 which was launched in April 2012), two are on the horizon: the Radarsat Constellation Mission (RCM), a fleet of three SAR systems scheduled for launch between 2014 and 2015, and DESDynI (Raney, 2009), which is currently delayed while NASA seeks partners. Even in the absence of CP data, several earth observation studies have been published over the last six years using CP data that have been simulated from quad-polarized data (Souyris et al., 2005; Raney, 2006). The majority of applications of CP SAR data have been terrestrial including crop classification (Souyris et al., 2005; Ainsworth et al., 2009), soil moisture estimation (Truong-Loi et al., 2009), vegetation characterization (Angelliaume et al., 2007; Lardeux et al., 2011), and land cover mapping (Ainsworth et al., 2009; Nord et al., 2009). As part of an ongoing effort to explore the use of CP data in maritime surveillance, in this study we report on the application of CP data to ship detection. We have previously reported the application of CP data to iceberg detection (Denbina and Collins, 2012).

There are many possible approaches to the analysis of CP image data summarized by Charbonneau et al. (2010) in his overview article. Planetary imaging applications have focused on the use of parameters derived from the CP Stokes vector (Charbonneau et al., 2010; Stacy and Campbell, 1993; Carter et al., 2011) and Raney advocates the use of this approach (Raney, 2006; Raney, 2007b). It will require an exploration of the information content of these parameters in a wide variety of applications. Another approach is to use the CP data to estimate components of the quad-polarized covariance matrix and use these reconstructed quad-pol data (termed pseudo-quad, or PQ, data) in existing quad-pol algorithms. This has been the approach taken by Souyris et al. (2005) and Nord et al. (2009) in two papers presenting quad-pol reconstruction algorithms. These algorithms have been developed in the context of terrestrial imaging. In a companion paper (Collins et al., 2012) we adapted the Souyris reconstruction algorithm for maritime surveillance and found excellent agreement between the PQ covariance matrix and observations.

Recently Yin et al. (2011) and Shirvany et al. (2012) have reported the first applications of CP to ship detection. Yin refined the Souyris reconstruction algorithm for complex targets (ships) by adding a helix scattering component to the covariance matrix model and changing the volume scattering component. He tested his reconstruction algorithm comparing the ship detection performance of the original quad-pol data, PQ data using the original Souyris algorithm and his own algorithm, and the raw CTLR dual-pol data. We will discuss his results later in this paper. Shirvany used the degree of polarization, a parameter derived from the Stokes vector, to detect ships. His results, although encouraging, were purely qualitative.

In addition to these two studies, Liu et al. (2010) in an internal technical document, reported ship detection performance results comparing, quad-pol, $|HH/HV|$, HH, and CTLR for ten ships in a Radarsat-2 FQ4 scene. She further explored the use of RH-RV dual polarized data for ship and iceberg detection (Liu et al., 2011). We will discuss their results in Section 6.

Notwithstanding these early successes for CP data for terrestrial applications, quad-pol reconstruction from CP data has been criticized from several quarters. Cloude (2009) investigated the reconstruction algorithm and found that the assumptions required were not consistent with observations. Cloude also developed a statistical test to determine if quad-pol data offer greater information content over CP data. His results for forested regions varied, while his results for a single region of ocean found that quad-pol data offered greater information. Touzi (2009) made qualitative evaluations of CP data for ship detection and wetland detection, and found the CP data could not replicate his limited quad-pol-based analyses. However, the proponents of hybrid polarity have never claimed that it is a replacement for quad-pol data. The major advantage of compact polarimetry over quad-pol data is that it offers double the swath width. Another advantage is that CTLR radar can easily adapt to the Scan-SAR imaging mode which will offer much more swath coverage than quad-pol system. This is a key issue for ocean surveillance.

The objective of our research is to explore the potential of CTLR compact polarimetry data in ship detection applications. We limit our attention, in this study, to the quad-pol covariance matrix reconstructed from simulated CTLR data, i.e. PQ data. Our CTLR data is simulated from Radarsat-2 fine-quad (FQ) data. We compare the performance of a likelihood ratio ship detection algorithm using PQ data versus the standard quad-, dual, and single-pol data. In Section 2 we discuss our data. In Section 3 we describe the reconstruction algorithm and in Section 4 we describe the implementation of a likelihood ratio ship detection algorithm to the reconstructed data. In Section 5 we explain our experimental methods and in Section 6 we present and discuss our results. Finally, in Section 7 we make concluding remarks.

2. Data and study site

The Radarsat-2 quad-pol data used in this study were acquired with the fine quad (FQ) beam mode over the Strait of Gibraltar. The scenes are shown in Table 1. The average wind speed in m/s (W.S.) calculated for each scene using the mean value of the HV radar backscatter coefficient (σ°) of ocean pixels, according to a model developed by Vachon and Wolfe (2011) is also provided.

The azimuth sample spacing for each scene is given in Table 1 and all scenes have a range sample spacing of 4.73 m. Nominal spatial resolution for Radarsat-2 fine quad mode is approximately 5.2 m in range by 7.6 m in azimuth. Radar backscatter coefficient (σ°) values were used for the calibration of the data.

Table 1
An overview of the Radarsat-2 data of the Strait of Gibraltar used in this study. 'The table shows the FQ beam number (Beam), scene acquisition date and time (Acq. Date/Time), incidence angle range covered by each beam (Inc. Angle), and the sample spacing in azimuth direction (Az. Spacing). WS is wind speed in meters/second. N.Ships is the number of ships we analyzed in each scene.

Scene No.	Beam	Acq. Date/Time	Inc. Angle (°)	Az. Spacing (m)	WS (m/s)	N.Ships
1	FQ4	2008-07-29/18:10:57	22.16–24.08	4.93	4.1	39
2	FQ8	2008-11-20/06:30:54	26.88–28.71	4.78	11.3	11
3	FQ12	2008-11-27/06:26:46	31.34–33.03	4.93	11.9	8
4	FQ21	2009-02-14/06:22:38	40.17–41.61	5.12	12.1	6

3. Reconstruction of quad-pol data from simulated CTLR data

The reconstruction of the quad-pol covariance matrix from simulated CTLR data is a two step process: (i) first simulate the CTLR from linearly polarized quad-pol data and (ii) reconstruct elements of the quad-pol covariance matrix. The algorithms we used are described in detail in a companion paper (Collins et al., 2012). Here we briefly summarize the process.

The original quad-pol scattering vector is,

$$\mathbf{X}_{\text{quad-pol}} = \begin{bmatrix} S_{HH} & \sqrt{2}S_{HV} & S_{VV} \end{bmatrix}^T \tag{1}$$

where we have applied the assumption of scattering reciprocity (which implies that $S_{HV} = S_{VH}$). It has been shown (Souyris et al., 2005; Nord et al., 2009) that CTLR CP data may be simulated from the measured quad-pol 2×2 scattering matrix by multiplying this scattering matrix by the right circular polarization Jones vector. The resulting CTLR scattering vector is,

$$\mathbf{X}_{\text{CTLR}} = \frac{1}{\sqrt{2}}\begin{bmatrix} S_{HH} - jS_{HV} & S_{HV} - jS_{VV} \end{bmatrix}^T \tag{2}$$

The CTLR covariance matrix may be written as a sum of three components,

$$\mathbf{C}_{CTLR} = \frac{1}{2}\left\langle \begin{bmatrix} |S_{HH}|^2 & i(S_{HH}\cdot S_{VV}^*) \\ -i(S_{VV}\cdot S_{HH}^*) & |S_{VV}|^2 \end{bmatrix} + \begin{bmatrix} |S_{HV}|^2 & -i|S_{HV}|^2 \\ i|S_{HV}|^2 & |S_{HV}|^2 \end{bmatrix} + \begin{bmatrix} -2\mathcal{I}(S_{HH}\cdot S_{HV}^*) & S_{HH}\cdot S_{HV}^* + S_{VV}^*\cdot S_{HV} \\ S_{HH}^*\cdot S_{HV} + S_{VV}\cdot S_{HV}^* & 2\mathcal{I}(S_{VV}\cdot S_{HV}^*) \end{bmatrix} \right\rangle \tag{3}$$

where T is the transpose operator, the angle brackets represent spatial averaging and $\mathcal{I}$ is the imaginary part of a complex number. In order to estimate the quad-pol 3×3covariance matrix, we must estimate nine unknowns. However we have only four equations from the CP mode covariance matrix. Thus, we must make some assumptions to constrain the solution space and reduce the number of unknowns and/or increase the number of equations. The original CP reconstruction algorithm (Souyris et al., 2005) starts with the assumption of reflection symmetry, which we have demonstrated is valid for ocean backscatter at C-band (Collins et al., 2012). Under this assumption, there is complete decorrelation of the co-polarized and the cross-polarized backscattering coefficients,

$$\langle S_{HH}\cdot S_{HV}^*\rangle = \langle S_{VV}\cdot S_{HV}^*\rangle = 0 \tag{4}$$

This assumption simplifies the PQ covariance matrix, by removing the third component, reducing the number of unknowns to five: $|S_{HH}|$, $|S_{HV}|$,$|S_{VV}|$ are real, and $(S_{HH}.S_{VV}^*)$ is complex.

To further constrain the solution, Souyris developed a general relation between the linear HH-VV coherence and the cross-polarization ratio (Souyris et al., 2005),

$$\frac{\langle |S_{HV}|^2\rangle}{\langle |S_{HH}|^2\rangle + \langle |S_{VV}|^2\rangle} = \frac{(1-|\rho|)}{N} \tag{5}$$

where ρ is the HH-VV coherence, defined as:

$$\rho \equiv \frac{\langle S_{HH}\cdot S_{VV}^*\rangle}{\sqrt{\langle |S_{HH}|^2\rangle \cdot \langle |S_{VV}|^2\rangle}} \tag{6}$$

These two equations are iteratively solved to estimate $|S_{HV}|^2$ and the linear coherence (ρ) (see Collins et al. (2012) for details). The other pseudo co-pol components (S_{HH},S_{VV}) intensities and their relative phase ($S_{HH}.S_{VV}^*$) are estimated directly from the covariance matrix elements of the CP mode and the estimated $|S_{HV}|^2$ value as follows:

$$|S_{HH}|^2 = 2C_{11} - |S_{HV}|^2 \tag{7}$$

$$|S_{VV}|^2 = 2C_{22} - |S_{HV}|^2 \tag{8}$$

$$S_{HH}\cdot S_{VV}^* = -i2C_{12} + |S_{HV}|^2 \tag{9}$$

Thus the covariance matrix of the pseudo quad-pol data derived from the CTLR CP mode can be written as,

$$\mathbf{C}_{\text{PQ}_{\text{CTLR}}} = \begin{bmatrix} 2C_{11} - |S_{HV}|^2 & 0 & -i2C_{12} + |S_{HV}|^2 \\ 0 & 2|S_{HV}|^2 & 0 \\ (-i2C_{12} + |S_{HV}|^2)^* & 0 & 2C_{22} - |S_{HV}|^2 \end{bmatrix} \tag{10}$$

where C_{11}, C_{12} and C_{22} are the elements of the CTLR covariance matrix.

The variable N in Eq. (5) is a crucial parameter in reconstructing the quad-pol covariance matrix. It depends mainly on the dominant scattering mechanism of the area under study. Souyris et al. (2005) used a constant value of 4 for N based on the assumption that volume scattering was the dominant scattering mechanism. Nord et al. (2009) defined a model for N as the ratio of the double-bounce backscatter to the cross-pol backscatter,

$$N = \frac{|S_{HH} - S_{VV}|^2}{|S_{HV}|^2} \tag{11}$$

In their algorithm N is estimated with a sliding window that compensates for the varying strength of double-bounce backscatter to accommodate scattering from urban areas. In our study the objective is to detect ships in a background of ocean "clutter", with little or no land. It is well known that backscatter from the ocean is well modelled by single bounce scattering, so neither the original reconstruction algorithm proposed by Souyris et al. (2005), which assumes volume scattering, nor the modified algorithm proposed by Nord et al. (2009), which compensates for the double bounce scattering, are consistent with C-band microwave backscattering from ocean. We have developed an empirical model for N that retains the basic logic behind the original Souyris algorithm, but estimates N directly from the data (Collins et al., 2012). We found that there is a strong and robust relationship between the mean $N(\overline{N})$ for ocean Radarsat-2 FQ scenes and the incidence angle of the scene. Fig. 1 shows a nonlinear regression of incidence angle against $\overline{N}$. The goodness of fit (r^2) of this model is 0.74. Thus in our work we estimate N from our model and follow the reconstruction algorithm outlined above.

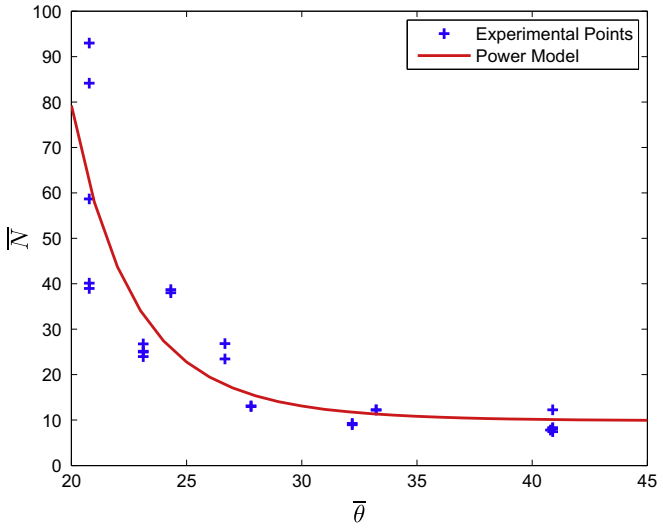

Fig. 1. Regression of the mean N values with mean incidence angle for Radarsat-2 FQ Gibraltar scenes. Blue crosses are the experimental points and red line is the power model $\overline{N} = 7.68 \times 10^{10}\ \theta^{-6.962} + 9.112$.

4. LRT ship detection algorithm

For the purpose of ship detection, the likelihood ratio test (LRT) with the Neyman-Pearson criterion developed by Liu et al. (2005) and Liu and Meek (2005) is applied to various SAR systems to distinguish between ship and ocean. The LRT is a pixel-based detection algorithm that maximizes the probability of detection at a specified false alarm rate (FAR). In the LRT algorithm, statistical decision theory is applied directly to the components of the scattering vector measured by the radar system for each pixel in an image to define a decision variable. The defined decision variable is then used to discriminate between ship and ocean samples by comparing it to a certain threshold at a specified false alarm rate.

4.1. Decision variable formation

In the LRT algorithm, a decision variable L is formed from the ratio of ship and ocean probability density functions. Under the assumption of Gaussian statistics for ships and ocean scattering components, the decision variable is given by:

$$L = X^H C_o^{-1} X = \left\{ \begin{matrix} > \eta & \text{for a ship} \\ \leqslant \eta & \text{for ocean} \end{matrix} \right\} \tag{12}$$

where $C_o = E\left(X_o X_o^H\right)$ is the ocean covariance matrix calculated for a region of the ocean, $E(\cdot)$ is the expectation operation over that region of the image, η is a threshold and X is the scattering vector for a pixel in the SAR image.

Eq. (12) is used for the determination of the decision variable for quad polarimetric systems and dual polarimetric systems with amplitude and phases by using appropriate definitions of X and the covariance matrices. For quad polarimetric data, X contains four elements and the inverse ocean covariance matrix is a 4×4 matrix. The decision variable is,

$$\begin{aligned} L_Q = {} & S_{HH}\left(S_{HH}^* C_{11} + S_{HV}^* C_{21} + S_{VH}^* C_{31} + S_{VV}^* C_{41}\right) \\ & + S_{HV}\left(S_{HH}^* C_{12} + S_{HV}^* C_{22} + S_{VH}^* C_{32} + S_{VV}^* C_{42}\right) \\ & + S_{VH}\left(S_{HH}^* C_{13} + S_{HV}^* C_{23} + S_{VH}^* C_{33} + S_{VV}^* C_{43}\right) \\ & + S_{VV}\left(S_{HH}^* C_{14} + S_{HV}^* C_{24} + S_{VH}^* C_{34} + S_{VV}^* C_{44}\right) \end{aligned} \tag{13}$$

where C_{ij} is the element of the ith row and jth column of the inverse ocean covariance matrix and $*$ is the complex conjugate operator. For a coherent dual-channel data, X is a vector with two elements

$$\mathbf{X} = [S_1 \quad S_2]^T \tag{14}$$

where S_1 and S_2 are the scattering components of the two polarimetric channels. The corresponding inverse ocean covariance matrix is a 2×2 matrix and the decision variable in Eq. (13) is reduced for coherent dual-pol data to

$$L_D = S_1\left(S_1^* C_{11} + S_2^* C_{21}\right) + S_2\left(S_1^* C_{12} + S_2^* C_{22}\right) \tag{15}$$

For the amplitude only dual channel data, where no phase information is available, the correlation between channels cannot be obtained from the amplitude data. In this case, the channels are assumed to be independent and the off diagonal elements of the ocean covariance matrix are set to zero. By substituting $C_{12} = C_{21} = 0$ in Eq. (15), the decision variable for these systems becomes,

$$L_D = |S_1|^2 C_{11} + |S_2|^2 C_{22} \tag{16}$$

For single channel systems, the scattering vector has a single element, S_1, and the decision variable for this system becomes

$$L_S = \frac{|S_1|^2}{E\left(|S_1|_o^2\right)} \tag{17}$$

Note that the denominator, $E\left(|S_1|_o^2\right)$, is calculated from a chosen ocean region while the numerator is calculated for each pixel in the image.

Recall that the reconstruction algorithm estimates only four elements of the quad-pol covariance matrix: the amplitude of the two co-pol components, their relative phase and the HV amplitude. Hence, we may consider that the PQ system is composed of two systems: the coherent HH-VV dual-pol system and the HV single-pol system. The decision variable for this system can be formulated by merging the decision variables of the coherent dual channel system and the single channel system (Eqs. (15) and (17)) as follows:

$$\begin{aligned} L_{PQ} = {} & S_{HH}\left(S_{HH}^* C_{11} + S_{VV}^* C_{21}\right) + S_{VV}\left(S_{HH}^* C_{12} + S_{VV}^* C_{22}\right) \\ & + \frac{|S_{HV}|^2}{E\left(|S_{HV}|_o^2\right)} \end{aligned} \tag{18}$$

In this equation, S_{HH}, S_{VV} and S_{HV} are the scattering components of the PQ data and C_{ij} is an element of the 2×2 ocean covariance matrix of the PQ HH-VV coherent system. After the calculation of the decision variable for all pixels in the image, the decision variable is compared to a threshold deduced from the measured variables (Liu et al., 2005; Liu and Meek, 2005) for ship detection. This threshold is specified at a desired FAR. If the decision variable exceeds the threshold, the pixel is a ship; otherwise it is ocean.

4.2. LRT detection performance

The detection performance of an LRT detector may be characterized with a plot of the receiver operating characteristics (ROC) (Liu et al., 2005; Liu and Meek, 2005; Scharf, 1990). The ROC curve is generated by plotting the probability of missed detection (PMD) versus the probability of false alarm (PFA) at various threshold values (Scharf, 1990). PMD and PFA are calculated as follows:

$$PMD = 1 - \frac{N_D}{N_S} \tag{19}$$

$$PFA = \frac{N_{FA}}{N_o} \tag{20}$$

where N_D is the number of detected pixels, N_S is the total number of ship samples, N_{FA} is the number of false alarms, and N_o is the total number of ocean samples in a specified area.

To compute the PFA for each system, a 1000×1000 pixel region of the ocean with no targets is selected. The decision variables for each pixel in the selected ocean-only region are calculated using ocean statistics. These decision variables are compared to a set of thresholds. For each threshold, if the decision variable is larger than the threshold, the pixel is considered a false alarm. To form the PFA at each threshold, the number of false alarms is divided by the total number of selected ocean pixels. For the same set of thresholds, the probability of detection (PD) values are computed as follows: first, one ship is selected from the image (after detection) and the decision variable for each ship pixel is recalculated using the ocean statistics. When the decision variable is higher than the threshold, the pixel is considered a detected pixel. The PD is computed by dividing the detected pixels by the total number of ship pixels and the PMD is calculated using (19). The ROC curve is plotted for each system using the (PFA, PMD) pairs.

5. Experimental methods

After simulating CTLR data from the observed FQ data, we reconstructed the quad-pol data as described in Section 3 using the appropriate value of N taken from the model shown in Fig. 1.

We identified 76 ships from the FQ beams corresponding to different incidence angles shown in Table 1. These are used to study the LRT detection performance of several quad-pol, dual-pol and single-pol SAR systems as a function of incidence angle. We compare the performance of observed quad-pol, dual-pol and single-pol systems to the simulated CTLR system and to several reconstructed quad-pol, dual-pol and single channel systems. The following systems are compared: Observed FQ: (quad-pol; coherent HH/VV; coherent and amplitude-only $|VV/VH|$; and HV); Simulated CTLR (coherent CTLR); and Reconstructed PQ ('full', coherent HH/VV, amplitude-only $|VV/VH|$; and HV).

This is a total of ten systems. We examine only the VV/VH dual-pol system as we found their performance was comparable to the HH/HV. We do not report the observed amplitude-only HH/VV as its performance was much weaker to the coherent HH/VV system.

Before applying the detectors to quad, dual and single channel FQ data, we spatially averaged the FQ data with a 5×5 boxcar filter. The averaging is performed on the Hermitian product of the scattering components (i.e. $S_i \cdot S_j^*$) used in calculating the decision variable for each SAR system and not on the complex scattering components. Averaging the scattering component products is equivalent to averaging the covariance matrix elements for each system. This is done to achieve a fair comparison with the PQ data since the reconstruction algorithm operates on the spatially averaged CTLR covariance matrix (which is averaged with same 5×5 boxcar filter) to produce the PQ data.

As there is no space to report and discuss 76 ROC curves, we summarize the performance results by reporting the PMD for a fixed PFA of 10^{-5}. We provide median ROC curves for each scene to illustrate performance as a function of both PMD and PFA.

We anticipate that the orientation of the ships with respect to the radar range direction might affect the detector performance, so we measured the orientation of each ship relative to the range direction, with 0° begin parallel to the range direction. We could not discriminate the bow from the stern so 0° is equivalent to 180° and 90° (perpendicular to the range direction and parallel to the azimuth direction) is equivalent to 270°. We also assume azimuthal symmetry, so 45° is equivalent to 135°. Thus, we measured angles between 0° and 90° to the nearest 10°.

We expect higher performance (lower PMD) for ship orientations of 90° and, to a lesser extent, 0°. At 90°, the ship is broadside to the radar range direction and offers the largest surface area facing the radar. At this angle, the hull and superstructure should generate a significant amount of double bounce and a higher radar cross section, thus a lower PMD. At 0° the ship offers the smallest surface area but its superstructure should also be roughly perpendicular to the range direction and we might see a slightly lower PMD than at other orientations. At all other angles, we would expect the radar pulse to be reflected away from the radar. Thus we are looking for enhanced performance (lower PMD) at 0° and 90°.

Rather than report the detection results for all 76 ships, we summarize detection results for all ships at a particular orientation reporting the median PMD and indicate the number of ships used for the calculation. We use the median since the sample sizes are small and the median is less affected by outliers.

6. Results

The summarized detection performance results are presented in Table 2. The detectors (columns) have been organized into three sets of columns corresponding to quad-pol, dual-pol and single-pol systems. The table is also organized into four sections according to incidence angle, from the steepest incidence angle beam (FQ4: 22.16° – 24.08°) at the top to the shallowest beam (FQ21: 40.17° – 41.61°) at the bottom. Each beam section contains ships identified in that single FQ scene. Within each scene, the rows refer to ships at a particular orientation, from 0° at the top to 90° (or the highest observed angle) at the bottom (an explanation of the orientation angles is given in the previous section). In some cases the orientation entry refers to the median result taken over several ships, in which case the orientation angle has a subscript indicating the number of ships. Where there is no subscript, the result refers to a single ship. Note that in a few cases we were not able to discern the orientation of a ship, and these ships do not appear in the results broken down by ship orientation for the scene. Thus the orientation subscripts do not sum to 76. Nevertheless, these ships were used in the calculation of the scene median and the overall median. The bottom row of each scene is the median detector result over all ships in that scene (the number of ships in each scene is given in Table 1) and the bottommost row in the table is the median detector performance over all 76 ships in our study. The grey shaded and bold face entries are discussed below.

The first discussion is the performance of the detectors as the incidence angle increases from FQ4 (22.16° – 24.08°) to FQ21 (40.17° – 41.61°), an increase in incidence angle of almost 20°. The FQ quad-pol detection performance improves slightly as the incidence angle increases. The FQ dual-pol and HV performance fluctuates, deteriorating at the shallowest incidence angle. The PQ detectors all have the strongest performance at the steepest incidence angle (FQ4), then deteriorate with incidence angle, with a spike of their weakest performance at FQ8. Several authors (Vachon et al., 1997; Askari and Zerr, 2000; Rey et al., 1996; Robertson et al., 2000; Gower and Skey, 2000) report that ship detection performance improves as incidence angle increases. However, the advantages of higher incidence angles are generally realized with higher winds (Gower and Skey, 2000) with more modest increases observed in moderate winds (Robertson et al., 2000). In our case, the winds are moderate in all four scenes, thus the slight performance gain we observed is consistent with the literature.

As discussed in the previous section, we expect enhanced performance (lower PMD) at 0° and 90°. PMD results at 0° that are lower than the next higher orientation angle and results at 90° that are lower than the next lower orientation angle are indicted in bold face as evidence of this effect. We can see that there are many cases

Table 2
Probability of missed detection (PMD) for several ships at a fixed probability of false alarm (PFA) of 10^{-5}. The leftmost column is the orientation of the observed ship in degrees estimated from the range direction of the radar, i.e. if the ship is oriented along the range direction, its orientation is 0°, while if it is oriented along the satellite track, its orientation is 90°. In several cases there were more than one ship at a particular orientation angle, in these cases the median detector permanence is shown. The orientation angles are subscripted with the number of ships used in the estimate. The lowest PMD is shaded in dark grey. In cases where the lowest PMD was achieved with the quad-pol data, the next lowest non-quad-pol detector is shaded with dark grey. Detectors whose PMD is within 0.02 of the lowest PMD are shaded with a lighter grey.

Ship Orient[n]	FQ Quad	PQ full PQ	FQ VV/VH	FQ |VV/VH|	FQ *HH/VV*	PQ CTLR	PQ *HH/VV*	PQ |VV/HV|	PQ *HV*	FQ *HV*
Scene 1: FQ4 22.16–24.08°										
0_4	0.13	**0.20**	0.31	0.26	0.50	0.17	**0.29**	0.11	0.10	0.21
10_7	0.12	0.24	0.20	0.20	0.46	0.15	0.30	0.09	0.05	0.13
15_3	0.26	0.40	0.33	0.29	0.65	0.44	0.47	0.32	0.27	0.24
20_3	0.16	0.30	0.28	0.28	0.64	0.21	0.34	0.18	0.07	0.20
30_5	0.22	0.29	0.28	0.24	0.56	0.25	0.32	0.20	0.15	0.21
45	0.13	0.18	0.15	0.15	0.44	0.17	0.22	0.12	0.11	0.12
50_2	0.11	0.17	0.09	0.16	0.41	0.11	0.20	0.10	0.07	0.08
90_4	0.11	**0.14**	**0.09**	0.23	**0.31**	**0.09**	**0.19**	**0.08**	**0.05**	0.20
Median	0.16	0.24	0.24	0.21	0.50	0.17	0.30	0.13	0.10	0.17
Scene 2: FQ8 26.88–28.71°										
0	0.20	0.31	0.27	0.26	0.76	0.30	**0.37**	0.25	0.24	0.22
25	0.17	0.30	0.20	0.19	0.68	0.30	0.40	0.23	0.22	0.16
30_2	0.22	0.37	0.32	0.31	0.71	0.33	0.45	0.31	0.30	0.25
40	0.14	0.31	0.16	0.16	0.58	0.26	0.39	0.25	0.24	0.10
55	0.32	0.42	0.33	0.32	0.63	0.41	0.44	0.39	0.38	0.29
60	0.08	0.15	0.12	0.12	0.67	0.11	0.19	0.11	0.11	0.09
90_2	0.11	**0.14**	0.22	0.22	**0.47**	**0.11**	**0.18**	0.33	**0.10**	0.21
Median	0.17	0.31	0.22	0.22	0.67	0.28	0.39	0.25	0.24	0.21
Scene 3: FQ12 31.34–33.03°										
0	**0.06**	**0.10**	**0.19**	**0.19**	**0.27**	-	**0.10**	**0.06**	**0.05**	**0.15**
10	0.39	0.47	0.45	0.45	0.58	0.44	0.49	0.44	0.42	0.41
20_2	0.26	0.33	0.48	0.34	0.63	0.30	0.35	0.32	0.28	0.28
30_2	0.17	0.25	0.33	0.25	0.44	0.21	0.28	0.21	0.18	0.21
45	0.09	0.13	0.13	0.13	0.49	0.13	0.14	0.22	0.14	0.10
90	0.12	0.21	0.21	0.21	0.38	0.17	0.24	**0.17**	**0.14**	0.17
Median	0.12	0.19	0.27	0.20	0.50	0.17	0.21	0.22	0.15	0.16
Scene 4: FQ21 40.17–41.61°										
0_3	**0.04**	**0.09**	**0.09**	**0.09**	**0.24**	**0.13**	**0.14**	**0.05**	**0.18**	**0.06**
17	0.15	0.32	0.34	0.34	0.40	0.19	0.36	0.22	0.21	0.32
20	0.12	0.25	0.22	0.22	0.41	0.20	0.30	0.19	0.17	0.20
25	0.29	0.42	0.40	0.40	0.56	0.34	0.46	0.36	0.33	0.37
Median	0.12	0.25	0.25	0.25	0.40	0.20	0.30	0.20	0.19	0.28
Median	0.17	0.27	0.29	0.28	0.55	0.20	0.31	0.20	0.15	0.21

where the 0° and 90° orientations have a lower PMD than the other orientations. At the two shallowest incidence angles, all 0° results appear enhanced, while for the two steepest angles, only one result is enhanced. The PMD for 90° orientations is enhanced for the majority of detectors in the two steepest incidence angles, but only a few for the FQ12 beam. However, the 90° results for this beam refer to a single ship.

The effect of ship orientation on ship detectability has been pointed out by Vachon et al. (1997) and Friedman et al. (2001). Margarit and his colleagues have integrated detailed ship and sea surface scattering models with a SAR simulation system (called GRECOSAR) that can model polarimetric backscatter as a function of the dynamic three-dimensional ship orientation (Margarit et al., 2009; Margarit and Tabasco, 2011). They note that the different polarimetric scattering mechanisms are mixed at spatial resolutions comparable to Radarsat-2 FQ and that the polarimetric backscatter, in this case, is very sensitive to incidence angle and backscatter (Margarit et al., 2009). Our results confirm that the performance of the LRT detector is a function of ship orientation, although it is a relatively weak effect.

Finally we come to the comparison of the FQ, PQ and CTLR detectors. In each row of the table, the detector with the lowest PMD, i.e. the highest performance is shaded with a dark gray. In cases where the highest performer is the observed quad-pol detector, the next lowest non-quad-pol detector is also shaded with a dark gray. To indicate detectors whose performance is "close" to the highest performer, detectors whose performance is within 0.02 of the lowest PMD, are shaded a lighter gray.

For the steepest FQ4 beam (22.16° – 24.08°) the highest median performance is by the PQ HV detector, higher in all but one of the orientation cases than the FQ quad-pol performance. At one orientation, 15°, the FQ HV detector had the highest performance.

For all other individual beams, the highest median performer was the FQ quad-pol detector. For the FQ8 beam, (26.88–28.71°), the FQ HV detector had the highest median non-quad-pol performance followed by the two FQ VV/HV detectors. The PQ HV beam was the next highest (but not within 0.02). For the FQ12 (31.34–33.03°) and FQ21 (40.17–41.61°) beams the PQ HV detector was the next highest performer to the FQ quad-pol detector. The FQ HV and CTLR detectors also performed well at these incidence angles.

The highest median detector performance over all 76 ships, taken over all ship orientations and all incidence angles, is the PQ HV detector, higher even than the FQ quad-pol detector. The reason for this is a weaker detection performance of the quad-pol data in the low incidence FQ4 beam.

The median ROC curves for each of our four scenes are shown in Fig. 2. The median is calculated over all ships in each scene. These curves illustrate the detection performance as a function of PFA. At FQ4, we can see that the PQ HV and PQ |*VV*/*HV*| detectors have the highest performance over all PFA. The results for FQ8 show that at PFA below about 10^{-4}, the PQ *HV* is the highest performer. Above

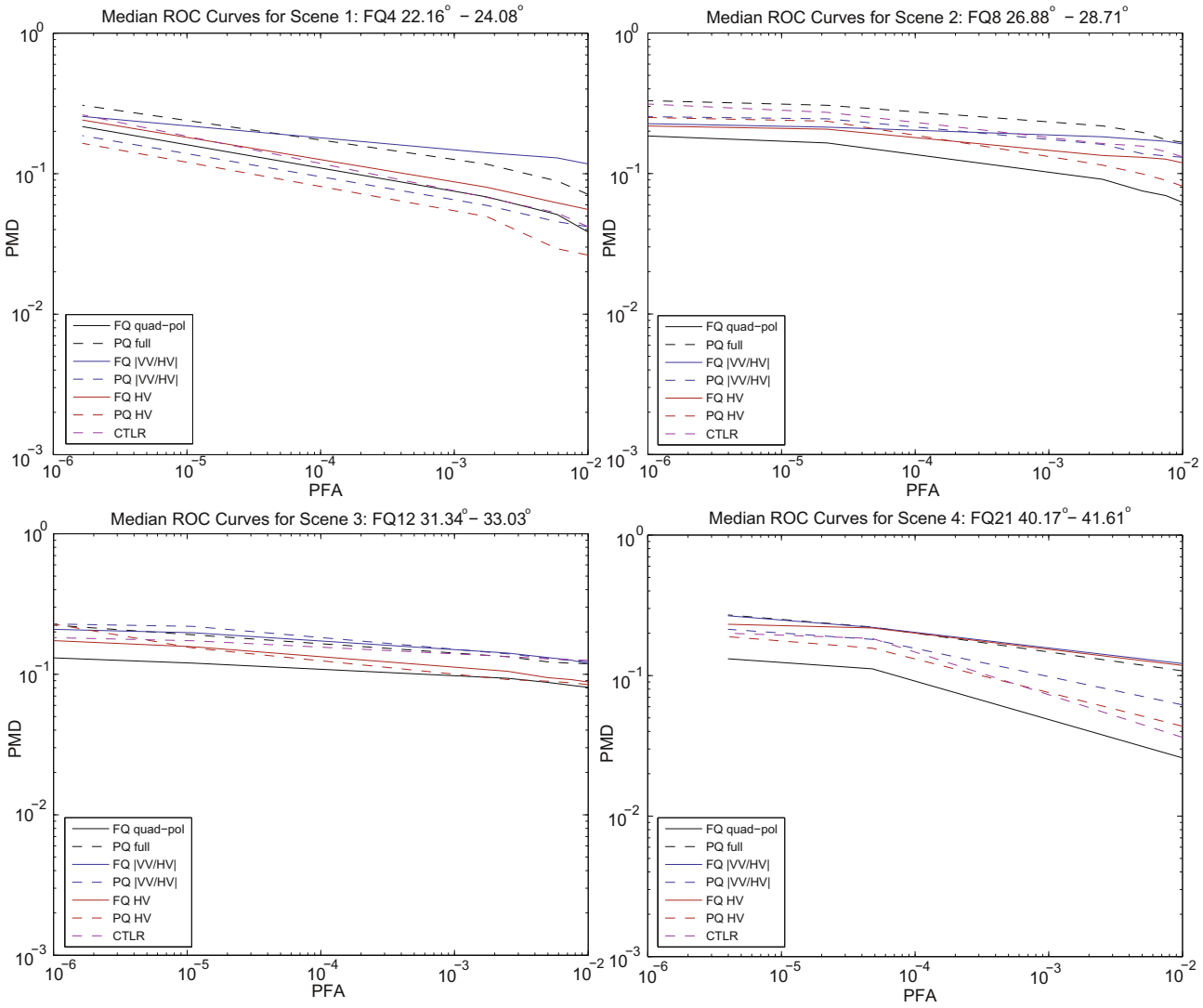

Fig. 2. Median ROC curves for the four scenes we investigated.

this value, the FQ-HV and FQ $|VV|HV|$ detectors have the highest performance. At FQ12, the performance of the PQ *HV* detector deteriorates steadily against PFA. It is the highest non-quad-pol detector at PFA of 10^{-5}, but is eclipsed by the FQ *HV* detector after this. Note that the coherent CTLR detector has relatively consistent performance against PFA coming very close to FQ *HV* at PFA 10^{-6}. At FQ21, the PQ *HV* and CTLR detectors have comparable performance below PFA 10^{-4}. At higher PFA, the PQ HV detector has the highest performance.

The ROC curves shows that the detection performance is a relatively weak function of PFA, and the differences in performance between the various detectors is generally small.

Note that in no case did the full PQ detector perform particularly well. The addition of the coherent *HH*|*VV* dual pol with the *HV* did not improve performance over the simple PQ *HV* detector in any case. The "native" CTLR detector had higher performance than the full-PQ detector in all cases.

As mentioned in Section 1, the majority of applications of simulated compact polarimetry data have been in studies of vegetation. Only two papers report the use of CP data for ship detection, one by Shirvany et al. (2012) and a second by Yin et al. (2011). Yin et al. (2011) presents two ROC curves, for two different data sources: JPL AIRSAR and SIR-C, presumably based on two individual ships. His ROC curves show the detection performance of the original quad-pol data, PQ data based on his refined algorithm, PQ data based on the original Souyris algorithm and the compact polarimetry data (in his case he simulated $\pi/4$ data). He did not explain how the LRT was implemented in these cases, thus we do not know whether the two PQ cases and the CP case were amplitude-only or if they are a sum of a coherent *HH*|*VV* and |*HV*|. Finally, we do not know what the incidence angles are for his two ships. In any event, we will assume that his CP detector is coherent and comparable to our own, except that it is $\pi/4$, and that his PQ detector contains the full reconstructed covariance matrix and is comparable to our full PQ detector. In both cases, the quad-pol detectors outperformed the PQ and CP detectors. For the AIRSAR case, the PQ and CP detectors have comparable performance while in the SIR-C case, the CP detector had much higher performance than the PQ case. Thus, although, he used $\pi/4$, our results are consistent with Yin's results in that detectors based on the coherent dual-pol compact polarimetry data have higher performance than those based on the full set of quad-pol covariance matrix elements reconstructed from the CP data.

Liu et al. (2010) also compared ship detection performance of quad-pol, dual-pol, single-pol and simulated CTLR data. They did not attempt to reconstruct PQ data and looked at a limited number

of dual-pol and single-pol cases: coherent *HH*|*HV* and *HH*. They used a single Radarsat-2 FQ4 scene of the Strait of Gilbraltar, examined the detection performance on ten ships and provided ROC plots for eight of these and a table of PMD values at PFA of 10^{-4} finding that in all cases, *HH* was the weakest performer and that the quad-pol detector was the strongest performer. In four of the eight ships, the dual-pol *HH*|*HV* detector had higher performance than the CTLR detector and in the remaining six ships, the CTLR detector had the next highest performance to the quad-pol detector. In two cases the CTLR detector performed quite close to the quad-pol detector. For our FQ4 scene, we found that the median performance of the quad-pol and CTLR detectors were comparable. Although, the median performance for some ship orientations of the FQ |*VV*|*HV*| detector was higher than the CTLR detector, it had a weaker performance over all ship orientations. Hence our results are consistent with Liu et al.

7. Conclusion

Our study provides the first comprehensive comparison of ship detection performance between several standard linear polarization combinations, CTLR compact polarimetry data, both the raw coherent dual pol CTLR data and reconstructed PQ data.

We have examined the effect of ship orientation and found that, while it does affect detection performance, the effect is weak, at least at the moderate wind speeds we have observed. We show that the detection performance of the quad-pol detector increased with incidence angle, while, for the other detectors, the performance either stayed the same or deteriorated as the incidence angle increased.

While the performance of all detectors fluctuated with ship orientation and with incidence angle, the PQ detectors provided consistently strong performance over all incidence angles. Based on Table 2 and the ROC plots in Fig. 2, the four strongest detectors were: quad-pol, *HV*, PQ *HV* and CTLR. The strongest median performer, over all incidence angles and ship orientations was the PQ *HV* detector, stronger even than the quad-pol detector. The standard linear *HV* detector also had very strong performance, except at the highest incidence angles. The ROC plots suggest that the CTLR detector can also be quite effective, particularly at low PFA.

These results suggest that CTLR compact polarimetry data and reconstructed PQ data have great potential for ship detection applications. Our results are limited to the relatively fine spatial resolution (5 m range by 8 m azimuth) of the Radarsat-2 fine-quad data. We are currently exploring maritime surveillance with CTLR data simulated using lower resolution beam modes from the upcoming RCM mission and with Stokes vector parameters derived from these data.

Acknowledgments

Paris Vachon of Defence Research and Development Canada provided both funding and data. Chen Liu, also of DRDC, helped us implement the LRT. We also acknowledge Francois Charbonneau, of the Canada Centre for Remote Sensing, for leading the Canadian working group on compact polarimetry. We further acknowledge funding support from Natural Science and Engineering Research Council (NSERC) of Canada.

References

Ainsworth, T., Kelly, J., Lee, J.-S., 2009. Classification comparisons between dual-pol, compact polarimetric and quad-pol SAR imagery. ISPRS Journal of Photogrammetry and Remote Sensing 64 (5), 464–471.

Angelliaume, S., Dubois-Fernandez, P., Souyris, J.-C., 2007. Compact polinsar for vegetation characterisation. In: Proc. IEEE International Geoscience and Remote Sensing Symposium (IGARSS). IEEE, pp. 1136–1138.

Askari, F., Zerr, B., 2000. Automatic Approach to Ship Detection in Spaceborne Synthetic Aperture Radar Imagery: An Assessment of Ship Detection Capability using RADARSAT. Technical Report SACLANTCEN-SR-338. SACLANT Undersea Research Centre, La Spezia, Italy.

Carter, L., Campbell, D., Campbell, B., 2011. Geologic studies of planetary surfaces using radar polarimetric imaging. Proceedings of the IEEE 99 (5), 770–782.

Charbonneau, F., Brisco, B., Raney, R., McNairn, H., Liu, C., Vachon, P., Shang, J., DeAbreu, R., Champagne, C., Merzouki, A., Geldsetzer, T., 2010. Compact polarimetry overview and applications assessment. Canadian Journal of Remote Sensing 36 (S2).

Cloude, S., 2009. Dual versus quadpol: a new test statistic for radar polarimetry. In: Proceedings of the Fourth International Workshop on Science and Applications of SAR Polarimetry and Polarimetric Interferometry – POLInSAR 2009. ESA SP-668.

Collins, M., Denbina, M., Atteia, G., 2012. On the reconstruction of quad-pol SAR data from compact polarimetry data for ocean target detection. IEEE Transactions on Geoscience and Remote Sensing 51 (1), 591–600.

D'Aria, D., Giudici, D., Guarnieri, A., Rizzoli, P., Medina, J., 2008. A wide swath, full polarimetric, L band spaceborne SAR. In: IEEE Radar Conference. pp. 1–4.

Denbina, M., Collins, M.J., 2012. Iceberg detection using pseudo quad-pol reconstruction of compact polarimetric SAR. Atmosphere Ocean 50 (4), 437–446.

Evans, D., 1979. Point target model for the synthetic aperture radar detection of ships and ice conditions during swell. IEEE Transactions on Antennas and Propagation 27 (1), 30–34.

Friedman, K., Wackerman, C., Funk, F., Pichel, W., Clemente-Colon, P., Li, X., 2001. Validation of a CFAR vessel detection algorithm using known vessel locations. In: Proceedings of the International Geoscience and Remote Sensing Symposium (IGARSS). pp. 1804–1806.

Gower, J., Hughes, J., 1979. Radar and ship observations of coastal sea surface roughness patterns in the Gelf of Georgia. In: Proceedings of the International Symposium on Remote Sensing of Environment, pp. 103–115.

Gower, J., Skey, S., 2000. Evaluation of RADARSAT ScanSAR for observing wind, slicks and fish-boats. Canadian Journal of Remote Sensing 26 (6), 484–493.

Greidanus, H., Clayton, P., Indregard, M., Staples, G., Suzuki, N., Vachon, P., Wackerman, C., Tennvassass, T., Mallorqui, J., Kourti, N., Ringrose, R., Melief, H., 2004. Benchmarking operational sar ship detection. In: Proc. IEEE International Geoscience and Remote Sensing Symposium (IGARSS), pp. 4215–4218.

Howell, C., Power, D., Lynch, M., Dodge, K., Bobby, P., Randell, C., Vachon, P., Staples, G., 2008. Dual polarization detection of ships and icebergs – recent results with ENVISAT ASAR and data simulations of Radarsat-2. In: Proc. IEEE International Geoscience and Remote Sensing Symposium (IGARSS), pp. 206–209.

Lardeux, C., Frison, P.-L., Tison, C., Souyris, J.-C., Stoll, B., Fruneau, B., Rudant, J.-P., 2011. Classification of tropical vegetation using multifrequency partial SAR polarimetry. IEEE Geoscience and Remote Sensing Letters 8 (1), 133–137.

Liu, C., Meek, A., 2005. Likelihood Ratio Test Polarimetric SAR Ship Detection Application. Defence Research and Development Canada, Technical Memorandum TM 2005-243.

Liu, C., Vachon, P.W., Geling, G.W., 2005. Improved ship detection with airborne polarimetric SAR data. Canadian Journal of Remote Sensing 31 (1), 122–131.

Liu, C., Vachon, P.W., English, R.A., Sandirasegaram, N., 2010. Ship Detection using RADARSAT-2 Fine Quad Mode and Simulated Compact Polarimetry Data. Defence Research and Development Canada, Technical Memorandum, TM 2009-285.

Liu, C., Vachon, P., Wolfe, J., 2011. Ship/iceberg detection using simulated compact polarimetry data. In: 8th Advanced SAR (ASAR) Workshop, 7–9 June, 2011, Saint-Hubert PQ.

Margarit, G., Tabasco, A., 2011. Ship classification in single-pol SAR images based on fuzzy logic. IEEE Transactions on Geoscience and Remote Sensing 49 (8), 3129–3138.

Margarit, G., Mallorqui, J., Fortuny-Guasch, J., Lopez-Martinez, C., 2009. Exploitation of ship scattering in polarimetric SAR for an improved classification under high clutter conditions. IEEE Transactions on Geoscience and Remote Sensing 47 (4), 1224–1235.

Nord, M., Ainsworth, T., Lee, J.-S., Stacy, N., 2009. Comparison of compact polarimetric synthetic aperture radar modes. IEEE Transactions on Geoscience and Remote Sensing 47 (1), 174–188.

Okada, Y., Hamasaki, T., Tsuji, M., Iwamoto, M., Hariu, K., Kankaku, Y., Suzuki, S., Osawa, Y., 2011. Hardware performance of L-band SAR system onboard ALOS-2. In: Proc. IEEE International Geoscience and Remote Sensing Symposium (IGARSS). pp. 894–897.

Olsen, R.B., Wahl, T., 2003. The ship detection capability of ENVISAT's ASAR. In: Proceedings of the International Geoscience and Remote Sensing Symposium (IGARSS). pp. 3108–3110.

Raney, R., 2006. Dual-polarized SAR and Stokes parameters. IEEE Geoscience and Remote Sensing Letters 3 (3), 317–319.

Raney, R., 2007a. Comments on hybrid-polarity SAR architecture. In: Proc. IEEE International Geoscience and Remote Sensing Symposium (IGARSS). IEEE, pp. 2229–2231.

Raney, R., 2007b. Hybrid-polarity SAR architecture. IEEE Transactions on Geoscience and Remote Sensing 45 (11), 3397–3404.

Raney, R., 2009. DESDynI adopts hybrid polarity SAR architecture. In: IEEE Radar Conference – Radar09, pp. 1–4.

Raney, R., Spudis, P., Bussey, B., Crusan, J., Jensen, J., Marinelli, W., McKerracher, P., Neish, C., Palsetia, M., Schulze, R., Sequeira, H., Winters, H., 2010. The lunar

mini-rf radars: hybrid polarimetric architecture and initial results. Proceedings of the IEEE 99 (5), 808–823.

Rey, M., Drosopoulous, A., Petrovic, D., 1996. A Search Procedure for Ships in RADARSAT Imagery. Report No.1305. Defence Research Establishment Ottawa, Canada.

Robertson, N., Bird, P., Brownsword, C., 2000. Ship surveillance using RADARSAT ScanSAR images. In: Alliance for Marine Remote Sensing (AMRS) Workshop on Ship Detection in Coastal Waters.

Scharf, L., 1990. Statistical Signal Processing: Detection, Estimation, and Time Series Analysis. Prentice Hall.

Shirvany, R., Chabert, M., Tourneret, J.-Y., 2012. Ship and oil-spill detection using the degree of polarization in linear and hybrid/compact dual-pol SAR. IEEE Journal of Selected Topics in Applied Earth Observations and Remote Sensing 5 (3), 885–892.

Souyris, J.-C., Imbo, P., rtoft, R.F., Mingot, S., Lee, J.-S., 2005. Compact polarimetry based on symmetry properties of geophysical media: the $\pi/4$ mode. IEEE Transactions on Geoscience and Remote Sensing 43 (3), 634–646.

Stacy, N., Campbell, D., 1993. Stokes vector analysis of lunar radar backscatter. In: Proc. IEEE International Geoscience and Remote Sensing Symposium (IGARSS), vol. 1. IEEE, pp. 30–32.

Swords, S., 1986. Technical History of the Beginnings of Radar. Institution of Engineering and Technology.

Touzi, R., 1999. On the use of polarimetric SAR data for ship detection. In: Proc. IEEE International Geoscience and Remote Sensing Symposium (IGARSS), pp. 812–814.

Touzi, R., 2000. Calibrated polarimetric SAR data for ship detection. In: Proc. IEEE International Geoscience and Remote Sensing Symposium (IGARSS), pp. 144–146.

Touzi, R., 2009. Compact-hybrid versus linear-dual and fully polarimetric SAR. In: Proceedings of the Fourth International Workshop on Science and Applications of SAR Polarimetry and Polarimetric Interferometry – POLInSAR 2009. ESA SP-668.

Touzi, R., Charbonneau, F., Hawkins, R.K., Kevin Murnaghan, K., Kavoun, X., 2001. Ship-sea contrast optimisation when using polarimetric SAR. In: Proc. IEEE International Geoscience and Remote Sensing Symposium (IGARSS), pp. 426–428.

Truong-Loi, M.-L., Freeman, A., Dubois-Fernandez, P., Pottier, E., 2009. Estimation of soil moisture and Faraday rotation from bare surfaces using compact polarimetry. IEEE Transactions on Geoscience and Remote Sensing 47 (11), 3608–3615.

Vachon, P., Wolfe, J., 2011. C-band cross-polarization wind speed retrieval. IEEE Geoscience and Remote Sensing Letters 8 (3), 456–459.

Vachon, P., Campbell, J., Bjerkelund, C., Dobson, F., Rey, M., 1997. Ship detection by the RADARSAT SAR: validation of detection model predictions. Canadian Journal of Remote Sensing 23 (1), 48–59.

Yeremy, M., Campbell, J., Mattar, K., Potter, T., 2001. Ocean surveillance with polarimetric SAR. Canadian Journal of Remote Sensing 27 (4), 328–344.

Yin, J., Yang, J., Zhang, X., 2011. On the ship detection performance with compact polarimetry. In: Proceedings of the IEEE Radar Conference (RADAR), pp. 675–680.